Critical phenomena in gravitational collapse with competing scalar field and gravitational waves, in 4+1 dimensions

Bernardo Porto Veronese

École Polytechnique, Route de Saclay, 91128 Palaiseau Cedex, France

Carsten Gundlach

Mathematical Sciences, University of Southampton, Southampton SO17 1BJ, United Kingdom

(Dated: 17 September 2022)

In the gravitational collapse of matter beyond spherical symmetry, gravitational waves are necessarily present. On the other hand, gravitational waves can collapse to a black hole even without matter. One might therefore wonder how the interaction and competition between the matter fields and gravitational waves affects critical phenomena at the threshold of black hole formation. As a toy model for this, we study the threshold of black-hole formation in 4+1 dimensions, where we add a massless minimally coupled scalar matter field to the gravitational wave ansatz of Bizón, Chmaj and Schmidt (in a nutshell, Bianchi IX on $S^3 \times$ radius $\times$ time). In order to find a stable discretisation of the equation governing the gravitational waves in 4+1 physical dimensions, which has the same principal part as the spherical wave equation in 9+1 dimensions, we first revisit the problem of critical spherical scalar field collapse in $n+2$ dimensions with large n. Returning to the main problem, we find numerically that weak gravitational wave perturbations of the scalar field critical solution decay, while weak scalar perturbations of the gravitational wave critical solution also decay. A dynamical systems picture then suggests the existence of a codimension-two attractor. We find numerical evidence for this attractor by evolving mixed initial data and fine-tuning both an overall amplitude and the relative strength of the two fields.

CONTENTS

I. INTRODUCTION

In many self-gravitating systems that are exactly scale-invariant, or asymptotically scale-invariant on small scales, numerical time evolutions of regular, finite mass initial data show that data which are fine-tuned more and more closely to the threshold of collapse, but otherwise generic, evolve into arbitrarily small black holes on the supercritical side of the threshold, arbitrarily large curvature before dispersion on the subcritical side. This is known as "type II critical phenomena in gravitational collapse", see [1] for a review.

The near-critical time evolutions go through a universal codimension-one attractor that is self-similar (or asymptotically self-similar on small scales), and which itself has a naked singularity, called the "critical solution". In the limit of perfect fine-tuning of any one parameter of the initial data to the collapse threshold, the time evolution approaches but never leaves the critical solution, and so a naked singularity is generated in the time evolution of a codimension-one set of otherwise generic initial data.

This is well established numerically, and well understood mathematically, for a number of Einstein-matter systems in spherical symmetry, see [1]. Moreover, for at least some of these systems, type II critical collapse is stable under small but finite non-spherical perturbations [2, 3]. Going beyond spherical symmetry is interesting for at least two reasons: it allows for angular momentum, and for gravitational collapse in vacuum.

Vacuum critical collapse is of interest as it is not tied to a particular choice of matter. However, fine-tuning to the threshold of collapse in vacuum gravity has proved numerically very difficult even in twist-free axisymmetry, see [4, 5] for the current state of the art. As a stepping stone from

vacuum, critical collapse has been investigated in twist-free axisymmetry with matter, in particular a perfect fluid [3] and electromagnetic radiation [6]. However, in going beyond spherical symmetry, the moving matter necessarily also creates gravitational waves. In the critical collapse of axisymmetric electromagnetic waves, an approximately discretely self-similar (from now on, DSS) critical solution was observed, but with scale-periodicity less regular than that observed in spherical scalar field collapse [6]. It was conjectured that this is due to the effect of strong gravitational waves.

As a spherically symmetric toy model for this interaction of matter and gravitational waves, one of us with collaborators [7] investigated critical collapse with two massless matter fields, a Yang-Mills (from now on, YM) and a scalar field. They found the well-known critical solutions for pure YM and pure scalar field matter. Perturbing pure initial data with an infinitesimal amount of the other type of matter, they established that weak YM perturbations of the scalar field critical solution decay, but that weak scalar perturbations of the YM critical solution grow.

Setting up mixed initial data with different ratios, and fine-tuning again to the black-hole threshold, they found a mixed-field critical solution that starts as a growing perturbation of the pure YM critical solution (at large scales) and ends as a decaying perturbation of the pure scalar critical solution (at small scales). This solution changes its matter content from pure YM to pure scalar field on the fly, while remaining very compact (with $2M/R \sim 0.5$) and approximately DSS, with the approximate log-scale period Δ changing from the YM to the scalar field value.

Here we investigate another toy model, where the two interacting fields truly are gravitational waves and a massless matter field. Bizón, Chmaj and Schmidt [8] proposed an ansatz in 4+1 spacetime dimensions on the manifold $S^3 \times (\mathbb{R} \times \mathbb{R}^+)$, where the metric on the factor S^3 is homogeneous but anisotropic, namely, it is of Bianchi type IX. Here all metric variables depend only on time and radius, even though the spacetime is vacuum. (This can be generalised to higher odd-dimensional spheres). To this system we simply add a homogeneous massless minimally coupled scalar field Ψ.

We thus have a toy model for matter coupled to gravitational waves, but where all fields depend only on radius and time, so that numerical time evolutions are cheap. Besides the unphysical dimensions, the major shortcoming of this model is that the scalar field cannot create gravitational waves if they are absent initially – we shall discuss this in more detail below.

The field equations for the scalar field and the gravitational waves are essentially spherical wave equations, in the physical 4+1 dimensions for the scalar field Ψ, but effectively in 9+1 dimensions for the gravitational wave variable b. As is well-known, such spherical wave equations are numerically difficult in high dimensions. It turns out the methods that work well in 3+1 dimensions stretch to 4+1 but not to 9+1 dimensions. As a stepping stone, we were therefore forced to revisit the problem of critical collapse of a spherically symmetric scalar field in high dimensions. In Appendix A we re-derive and modify the method of [9] and present successful tests in critical scalar field collapse in 9+1 (physical) dimensions.

In Sec. III we present our discretisation of the field equations, using the methods of Appendix A for the field b, and in Sec. IV the similarity coordinates that we use to display the approximate self-similarity of near-critical time evolutions. Sec. V contains our numerical results, and Sec. VI our conclusions.

II. METRIC ANSATZ AND FIELD EQUATIONS

We make the Bianchi IX ansatz of [8], restricting to the biaxial case. We introduce null coordinates adapted to the Bianchi IX symmetry $(u, x, \theta, \varphi, \psi)$, in terms of which the line element becomes

$$ds^2 = -2G\,du\,dx - H\,du^2 + \frac{1}{4}R^2\Big(e^{2B}\,d\theta^2$$
$$+(e^{2B}\cos^2\theta + e^{-4B}\sin^2\theta)\,d\varphi^2$$
$$-2e^{-4B}\sin\theta\,d\varphi\,d\theta + e^{-4B}\,d\psi^2\Big). \quad (1)$$

The coordinate u is null, and the tangent vector to the affinely parameterised outgoing null geodesics ruling the surfaces of constant u is $U^a := -\nabla^a u = G^{-1}(\partial_x)^a$. Here G, H, R and B are functions of u and x only. We also introduce the derivative operator

$$\Xi := \partial_u - \frac{H}{2G}\partial_x, \quad (2)$$

which is tangential to the ingoing null rays emanating from the 3-surfaces of constant u and x. In the special case $H = 0$, x is also a null coordinate and $\Xi = \partial_u$.

We fix the remaining coordinate freedom in the ansatz (1) by imposing

$$\frac{H}{2G} = \left(1 - \frac{x}{x_0}\right)\frac{1}{2R_{,x}(u,0)}, \quad (3)$$
$$G(u,0) = R_{,x}(u,0), \quad (4)$$
$$R(0,x) = \frac{x}{2}. \quad (5)$$

This puts the centre $R = 0$ at $x = 0$, makes u the proper time there, and makes $x = x_0$ an ingoing

null surface. More generally, surfaces of constant x are timelike for $0 \leq x < x_0$ and spacelike for $x > x_0$. In particular, choosing the outer boundary of our numerical domain at $x = x_{\max} > x_0$ means that this boundary is future spacelike and no boundary condition is required.

Moreover, if x_0 is chosen so that the ingoing lightcone $x = x_0$ is approximately the past lightcone of the accumulation point $(u_*, 0)$ of scale echoes of an (approximately) self-similar spacetime, our coordinate system automatically zooms in on this point, giving us good resolution in critical collapse without the need for explicit mesh refinement.

Our coordinate x can be related to an ingoing null coordinate v by

$$v(u, x) = -f(u)\left(1 - \frac{x}{x_0}\right), \qquad (6)$$

where

$$f(u) = \exp\left[-x_0 \int_0^u \frac{du'}{2R_{,x}(u', 0)}\right]. \qquad (7)$$

v is an increasing linear function of x, such that $v = 0$ is mapped to $x = x_0$. Our coordinate system can therefore be thought of as a continuous version of Garfinkle's algorithm [10], which rescales v linearly in what in our notation is called x, but by interpolation at discrete moments of time u, rather than the continuous use of a radial shift vector. We had previously used Garfinkle's method in [6], and for that problem our new algorithm gives the same accuracy and run times. We have made the change here as it simplifies convergence testing. Both algorithms require a good choice of, in our notation, x_0 in order to make the coordinate system zoom in on the accumulation point of critical collapse.

To regularise the field equations, we redefine two of the metric coefficients as

$$B =: R^2 b \qquad (8)$$

and

$$G =: R_{,x} g. \qquad (9)$$

There are four algebraically independent components of the Einstein equations

$$R_{ab} = 8\pi \nabla_a \Psi \nabla_b \Psi. \qquad (10)$$

(We work in units where $G = c = 1$.) From these, we select one which is an ordinary differential equation for g on the slices of constant u, and two which are wave quations for R and b. The remaining Einstein equation is then redundant. We also have a wave equation for the matter field Ψ.

The four field equations thus obtained can be arranged in the following hierarchy:

$$\mathcal{D}(\ln g) = \frac{8\pi R}{3}(\mathcal{D}\Psi)^2$$
$$+ 2R^3(\mathcal{D}b + 2Rb)^2, \qquad (11)$$

$$\mathcal{D}(R^2 \Xi R) = \frac{gR}{3}(1 - 4e^{6bR^2})e^{-8bR^2}, \qquad (12)$$

$$\mathcal{D}(R^{3/2}\Xi\Psi) = -\frac{3}{2}\Xi R R^{1/2}(\mathcal{D}\Psi), \qquad (13)$$

$$\mathcal{D}(R^{7/2}\Xi b) = \frac{2}{3}gR^{-1/2}e^{-8bR^2}\left(1 - e^{6bR^2}\right.$$
$$+ bR^2(4e^{6bR^2} - 1)\Big)$$
$$- 4bR^{3/2}\Xi R - \frac{7}{2}R^{5/2}\Xi R\mathcal{D}b. (14)$$

Here

$$\mathcal{D}f := \frac{f_{,x}}{R_{,x}}, \qquad (15)$$

so that $\mathcal{D}$ is d/dR along the null geodesics ruling the slices of constant u. Note that these equations do not explicitly contain H. Rather, H can be chosen freely [we choose (3)], and appears only when we use

$$\Psi_{,u} = \Xi\Psi + \frac{H}{2G}\Psi_{,x} \qquad (16)$$

in order to advance Ψ in u, and similarly for b and R.

Eqs. (11-14) can be solved for g, ΞR, $\Xi\Psi$ and Ξb in the above order by the integration

$$\mathcal{I}f := \int f R_{,x}\, dx = \int f\, dR \qquad (17)$$

along the outgoing null geodesics, labelled by constant $(u, \theta, \varphi, \psi)$, starting the integration from the centre $R = 0$. Because of factors of R, three of the startup conditions are selected by regularity at $R = 0$. The fourth startup condition at $R = 0$ is the gauge choice $g = 1$, equivalent to (4) above.

This selection and hierarchical arrangement of the field equations closely resembles the form of the field equations for the spherical scalar field and YM field of [7], with ∂_u replaced by its generalisation Ξ. Somewhat less closely, it also resembles the formulation for the spherical scalar field of [10–12] (but with $\mathcal{D}$ and Ξ applied to Ψ in the opposite order), and the scheme of [13] for the vacuum Einstein equations on null cones with a regular vertex (but in terms of null coordinates u and x, rather than Bondi coordinates u and R).

In analogy with the field redefinitions made in [9] (see also Appendix A) we replace b as an evolved variable by

$$\chi := b + \frac{2}{7}R\mathcal{D}b, \qquad (18)$$

from which we can reconstruct b as

$$b = \frac{1}{R^{7/2}} \int_0^R \chi \, d(\tilde{R}^{7/2}). \qquad (19)$$

The computation of b from χ is more stable numerically if we integrate (19) by parts, giving us

$$b = \chi - \frac{2}{9} \frac{1}{R^{7/2}} \int_0^R \mathcal{D}\chi \, d(\tilde{R}^{9/2}). \qquad (20)$$

The second term on the right-hand side of Eq. (20) is $O(R)$ near the origin, and thus generates less error from finite differencing than the original integral in Eq. (19), which is $O(1)$ there.

The evolution equation for χ is

$$\Xi\chi = \frac{4}{21} \frac{g}{R^3} \Gamma(bR^2) - \frac{8}{7} \frac{b}{R} \left(\Xi R + \frac{g}{2} \right)$$
$$- \frac{(\chi - b)}{2R} \left[\Xi R + \frac{2g}{3} (1 - 4e^{6bR^2}) e^{-8bR^2} \right], \qquad (21)$$

where $\Gamma(x) := 3x + e^{-8x}(1 - e^{6x} + x(4e^{6x} - 1))$. Its series expansion is $\Gamma(x) = 30x^2 + O(x^3)$, and so the leading $b^2 R^4$ term near the origin cancels the first denominator of Eq. (21).

Furthermore, the expression $\Xi R + g/2$, which appears in the second term of Eq. (21), is $O(R^2)$ near the origin. This cancels the denominator of the second term. To see this explicitly, manifestly cancel the $O(1)$ and $O(R)$ contributions in ΞR and $g/2$ by integrating Eq. (12) by parts, giving us

$$\Xi R - \frac{g}{6} (1 - 4e^{6bR^2}) e^{-8bR^2}$$
$$= -\frac{1}{R^2} \int_0^R \frac{g\tilde{R}^3}{6} \left[\frac{8\pi}{3} (\mathcal{D}\Psi)^2 \right.$$
$$+ 2\tilde{R}^2 (\tilde{R}\mathcal{D}b + 2b)^2$$
$$\left. + 8(\tilde{R}\mathcal{D}b + 2b)(1 - e^{-6b\tilde{R}^2}) e^{-2b\tilde{R}^2} \right] d\tilde{R}. \qquad (22)$$

The left hand side equals $\Xi R + g/2 + O(R^4)$, and from the regularity of Ψ and b the integral on the right hand side is $O(R^4)$. [We do not use Eq. (22) in our code. It is given here just to show that Eq. (21) is explicitly regular.]

Finally, the regularity of the last term on the right hand side of Eq. (21) follows from the definition of χ, Eq. (18).

We now introduce some diagnostics. We define the Misner-Sharp-like quasilocal mass function $M(u, x)$, and the related compactness $\mathcal{C}$, by

$$\mathcal{C} := \frac{M}{R^2} := 1 - \nabla_a R \nabla^a R = 1 + 2\frac{\Xi R}{g}. \qquad (23)$$

In spherical symmetry, a marginally outer-trapped surface (from now on also referred to as an apparent horizon), occurs where $\mathcal{C} = 1$, but our formulation of the Einstein equations does not allow us to

reach this. Rather, we take $\mathcal{C} \to 1$ as an approximate criterion for apparent horizon formation.

For the diagnosis of subcritical scaling we introduce the curvature-like quantities

$$R_\Psi := R^a{}_a = 8\pi \nabla^a \Psi \nabla_a \Psi = -\frac{16\pi}{g} \Xi\Psi\mathcal{D}\Psi,$$
$$\qquad (24)$$

$$R_B := 6\nabla^a B \nabla_a B = -\frac{12}{g} \Xi B \mathcal{D}B$$
$$= -\frac{12}{g} (R^2 \Xi b + 2R\Xi Rb)(R^2 \mathcal{D}b + 2Rb). \qquad (25)$$

R_Ψ is actually the Ricci scalar, which is determined by Ψ alone, while B does not contribute to the Ricci tensor at all. However, Ψ and B appear in a similar manner both in the Einstein equation for g, namely

$$\mathcal{D}(\ln g) = \frac{2R}{3} \left(4\pi(\mathcal{D}\Psi)^2 + 3(\mathcal{D}B)^2 \right) \qquad (26)$$

[compare Eq. (11)], and in the mass aspect, namely

$$\mathcal{D}M = \frac{2R}{3} \left[3 + e^{-8B} - 4e^{-2B} \right.$$
$$\left. + (R^2 - M) \left(4\pi(\mathcal{D}\Psi)^2 + 3(\mathcal{D}B)^2 \right) \right]. (27)$$

We have adjusted the overall constant factor in the definition of R_B to reflect this. Note that R_Ψ is nonzero at the centre, whereas $R_B \sim R^2$ vanishes there.

Even though B represents genuine gravitational waves, their polarisation is in the angular, homogeneous, directions (θ, φ, ψ), while the scalar field depends only on the orthogonal directions (u, x). Therefore the scalar matter field cannot create gravitational waves if they are absent initially, in contrast to the case of electromagnetic waves, or a non-spherical scalar field or fluid, in 3+1 dimensions. In this respect, the system looks mathematically more similar to that of [7] (two matter fields coupled to each other only through the metric) than to, say, a massless scalar field minimally coupled to gravity in axisymmetry.

III. NUMERICAL METHOD

Our numerical implementation is an adaptation of that of [7]. We represent our fields on a grid with $N_x = 600$ equally spaced points in x, and numerically advance in the retarded time u. We set $x_i = i\Delta x$ for $1 \leq 1 \leq N_x$, with $x = 0$ not on the grid. We extrapolate to $x = 0$ where needed, and for output only, but we use the assumption that $R = 0$ there in our boundary conditions.

4

At every time step, we solve for b, g and the ingoing null derivatives ΞR, $\Xi\Psi$ and $\Xi\chi$ from (20), the integrated versions of Eqs. (11-13), and (21), in this order. We then evolve R, Ψ and χ from u to $u+\Delta u$ using a second-order Runge-Kutta method. We use the heuristic timestep criterion

$$|\Xi R|\Delta u \leq C R_{,x}\Delta x, \qquad (28)$$

implemented as

$$\Delta u = C \min_i \frac{2(R_i - R_{i-1})}{\max(\Xi R_i, \Xi R_{i-1})}. \qquad (29)$$

C is a dimensionless factor of order unity, as in [7]. We use $C = 0.1$ throughout.

To start up the integration of the Einstein equations, we make the least-squares fit $\Psi \simeq \Psi_0 + \Psi_1 R + \mathcal{O}(R^2)$ to the two innermost grid points. We then substitute these expansions into the integral expressions for g, ΞR, $\Xi\Psi$ and $\Xi\chi$, obtaining

$$g = 1 + \frac{4\pi\Psi_1^2}{3}R^2 + \mathcal{O}(R^3), \qquad (30)$$

$$\Xi R = -\frac{1}{2} - \frac{\pi\Psi_1^2}{3}R^2 + \mathcal{O}(R^3), \qquad (31)$$

$$\Xi\Psi = \frac{\Psi_1}{2} + \mathcal{O}(R). \qquad (32)$$

These expansions are used at the first grid point to start up the integrations for g, ΞR and $\Xi\Psi$. No linear expansion is required for $\Xi\chi$ as there is no integral.

The derivative $\mathcal{D}$ is discretised by symmetric finite differencing with respect to R:

$$(\mathcal{D}\Psi)_i = \frac{\Psi_i - \Psi_{i-1}}{R_i - R_{i-1}}, \qquad (33)$$

and likewise for χ and b. Indicating by

$$\bar{\Psi}_i = \frac{\Psi_i + \Psi_{i-1}}{2} \qquad (34)$$

the numerical approximation of Ψ in the midpoint of the i-th grid cell (and likewise for other quantities), the integrals over the grid points $1,\ldots,j$ are then discretised using the midpoint rule:

$$\int_{R_1}^{R_j} f(\Psi, \mathcal{D}\Psi, \ldots)\, d(\tilde{R}^\alpha)$$
$$\simeq \sum_{i=2}^j f(\bar{\Psi}_i, (\mathcal{D}\Psi)_i, \ldots)(R_i^\alpha - R_{i-1}^\alpha), \quad (35)$$

where $f(\ldots)$ is a placeholder for the right-hand sides of (20) and the integrated versions of Eqs. (11-13), and we use $\alpha = 9/2, 2, 2, 3/2$, respectively, in these equations. We use this discretisation of the integration measure because of its lower error near the origin compared with dR.

Because our finite-differencing scheme is second-order accurate in Δx, we expect any output to also converge to second order at sufficiently early time. We have checked convergence with a sequence $N_k := N_0 \cdot 2^k$ of resolutions with $N_0 = 100$ and $k = 0\ldots4$. Denoting by Z_k the output of the code for fixed initial data and N_k grid points, we expect the quantity $\Delta Z_k = 4^k \cdot (Z_{k+1} - Z_k)$ to be approximately independent of k.

We found pointwise convergence to second order in Δx in the bulk of the grid, except near the origin. The error at the first gridpoint was found to be approximately first-order. We have not found a stable way of improving on this. The transition to second order is illustrated in Fig. 1.
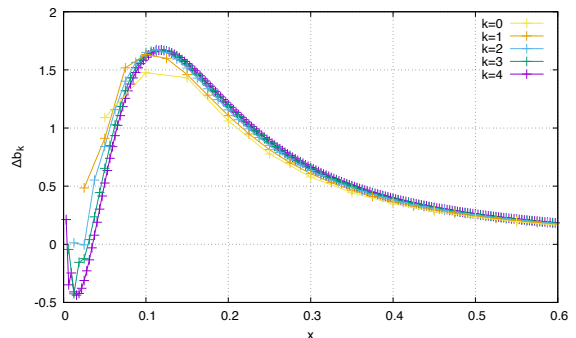
FIG. 1. The scaled error Δb_k for $k = 0\ldots4$, represented for $0 \leq x \leq 0.6$ and at a particular time instance $u = 0.444$ for centered Gaussian pure gravitational wave initial data with $b(0,x) = 13.88\exp[-(x/0.25)^2]$. While the curves progressively coincide for $x \gtrsim 0.2$, they differ slightly at the first grid points, although some (slower) convergence is still noticeable.

The computation of the function $\Gamma(x)$, which appears in Eq. (21), is done by performing a Taylor expansion up to 7th order once its argument satisfies $bR^2 \leq 0.01$. This way, its zeroth and first order terms are manifestly cancelled, avoiding numerical error near the origin from using the full expression for Γ.

We diagnose the formation of a marginally outer-trapped surface by comparing the maximum over one moment of time u of the compactness $\mathcal{C} := M/R^2$, defined by Eq. (23), to a fixed threshold $\mathcal{C}_{\max} = 0.999$. Similarly, we diagnose dispersion if the maximum of the compactness over the slice of constant u becomes smaller than $\mathcal{C}_{\min} = 0.001$.

IV. SIMILARITY COORDINATES

In any coordinates $x^\mu := (T, \xi, \theta, \varphi, \psi)$ adapted to the Bianchi symmetry and to DSS, by definition a spacetime is DSS if and only if the metric takes

the form

$$g_{\mu\nu} = e^{-2T}\tilde{g}_{\mu\nu}, \qquad (36)$$

where $\tilde{g}_{\mu\nu}$ is periodic in T with some period Δ. In particular, the area radius R must take the form

$$R = e^{-T}\hat{R}, \qquad (37)$$

with $\hat{R}$ again periodic. A scalar-field Ψ whose stress-energy tensor is compatible with this metric must itself be periodic in T with the same period.

We now introduce the specific DSS-adapted coordinates

$$T := -\ln\left(\frac{u_* - u}{k}\right) \qquad (38)$$

$$\xi := \frac{R}{u_* - u} = \frac{R}{k}e^{-T} \qquad (39)$$

for a constant $u_* > 0$ and $u < u_*$. (For $u > u_*$, both ξ and T are undefined). The constant k is a length scale which we set to 1. From Eq. (1) it is clear that the metric in coordinates (ξ, T) is of the form (36), and that the spacetime is DSS if and only if g, $\hat{R}$ and B are periodic in T.

When either $\Psi(0, x) = 0$ or $B(0, x) = 0$, we expect all dimensionless physical quantities, such as Ψ or B and M/R^2, to be periodic in T while the spacetime approximates the critical solution. We also expect dimensionful quantities to scale as e^{-lT}, where l is their length dimension. Thus, in the pure scalar field critical solution, R_Ψ behaves as e^{2T} times a periodic function of T (at constant x), and in the pure gravitational wave critical solution, R_B is e^{2T} times a periodic function of T.

V. NUMERICAL RESULTS

A. Initial data

We choose the 2-parameter family of Gaussian initial data (with parameters p and q)

$$\Psi(0, x) = p(1 - q)A_{(\Psi)}$$
$$\exp\left[-\left(\frac{R - \mu_{(\Psi)}}{w_{(\Psi)}}\right)^2\right], \qquad (40)$$

$$\chi(0, x) = pqA_{(\chi)}\exp\left[-\left(\frac{R - \mu_{(\chi)}}{w_{(\chi)}}\right)^2\right], \quad (41)$$

as well as a two-parameter family with the profile of the derivative of a Gaussian function:

$$\Psi(0, x) = -2p(1 - q)A_{(\Psi)}\left(\frac{R - \mu_{(\Psi)}}{w_{(\Psi)}^2}\right)e^{-\left(\frac{R - \mu_{(\Psi)}}{w_{(\Psi)}}\right)^2},$$
$$(42)$$

$$\chi(0, x) = -2pqA_{(\chi)}\left(\frac{R - \mu_{(\chi)}}{w_{(\chi)}^2}\right)e^{-\left(\frac{R - \mu_{(\chi)}}{w_{(\chi)}}\right)^2}.$$
$$(43)$$

Here $pqA_{(\Psi)}$ and $p(1 - q)A_{(\chi)}$ are the amplitudes, $w_{(\Psi)}$ and $w_{(\chi)}$ are the widths, and $\mu_{(\chi)}$ and $\mu_{(\Psi)}$ the centres of the Gaussians. The free initial data for the evolved variables are completed by Eq. (5) above.

The field equations, with the gauge boundary condition $g = 1$ at the centre, are scale-invariant in the sense that they do not change when we replace the arguments (u, x) of G (or g), R, B (or b) and Ψ by $(\lambda u, \lambda x)$, and the value of R by λR and of b by $\lambda^{-2}b$, but leaving the values of G (or g), B and Ψ unchanged. Put simply, everything scales according to its dimension, with u, x and R having dimension length, b having dimension (length)$^{-2}$ and B, G, g and Ψ being dimensionless. We fix this overall scale freedom by always setting the outer boundary of the grid to $x_{\max} = 8$.

For a fixed value of q, we start the bisection in p with a large value of x_0 close to $x_{\max}$, adjusting it manually and restarting the procedure until all individual simulations retain good spatial resolution throughout their evolution. This is done by keeping track of the grid point index of the location of the apparent horizon formed in the supercritical steps: if x_0 is too large, the horizon is formed at small x and the dynamics are not well resolved spatially. If x_0 is too small and for sufficient fine-tuning, the apparent horizon is formed outside the spatial grid.

After some experimentation, we choose widths, centers and amplitudes

$$\begin{aligned}
A_{(\chi)} &= 1.0, & A_{(\Psi)} &= 0.01, \\
\mu_{(\chi)} &= 0.5, & \mu_{(\Psi)} &= 1.15325, \\
w_{(\chi)} &= 0.05, & w_{(\Psi)} &= 0.115325
\end{aligned} \qquad (44)$$

for the Gaussian initial data and

$$\begin{aligned}
A_{(\chi)} &= 0.023, & A_{(\Psi)} &= 0.034, \\
\mu_{(\chi)} &= 0.74, & \mu_{(\Psi)} &= 1.22, \\
w_{(\chi)} &= 0.074, & w_{(\Psi)} &= 0.224
\end{aligned} \qquad (45)$$

for the Gaussian derivative initial data. These have the following properties:

1. For pure scalar initial data $q = 0$ and pure gravitational wave initial data $q = 1$, the critical

amplitudes are $p \simeq 1$. This is essentially a matter of convenience.

2. For the two pure initial data sets the accumulation point of echos at $R = 0$, $u = u_*$, $v = v_*$ is at a similar value of v_*. This is achieved in practice by independently finding the approximate value of $x_0 \simeq v_*$ for two sets of initial data corresponding to pure scalar field and pure gravitational waves, and then rescaling the scalar field initial data such that the two values of x_0 coincide.

This ensures that when we choose values of q representing a mixture of the two fields and then fine-tune p again to the threshold of collapse, we can expect the fields to interact strongly. By contrast, if v_* was much smaller for, say, the scalar field, in fine-tuning p for mixed data to the threshold of collapse, we would be likely to find critical collapse dominated by the scalar field, with the gravitational waves arriving later and either dispersing or forming a large black hole.

All plots in the following correspond to the Gaussian initial data, except for Fig. 19, which compares results from the two families.

For given q, we perform 50 bisection steps from a rough initial bracket for $p_*(q)$ to determine its value up to machine precision. We work in double precision. With $p_*(q)$ known (for a given set of numerical parameters such as x_0, $x_{\max}$, C and Δx) the scaling laws are then re-evaluated on 450 evenly spaced points in $\log_{10} |p - p_*|$, with 30 points per decade, to resolve for the fine structure of the DSS scaling, which we expect to be periodic with period $\Delta/(\ln(10)\gamma)$ in $\log_{10} |p - p_*|$.

B. The pure field cases

The mass and curvature scaling laws obtained for pure scalar field ($q = 0$) and pure gravitational wave ($q = 1$) initial data give critical exponents $\gamma_\Psi \simeq 0.415$ and $\gamma_B \simeq 0.164$ respectively, which agree with the results found in [9] and [8], respectively.

The echoing periods Δ [in T, defined above in Eq. (38)] of the best near-critical solutions were estimated by identifying the period with that of the Fourier mode of highest peak of Ψ or B, and then fitting the curves by eye with a sine wave of the same period. We determined $\Delta_\Psi \simeq 1.6$ and $\Delta_B \simeq 0.47$, in agreement with the values found in [9] and [8].

C. Gravitational waves with small scalar field perturbation

We now add a small perturbation $\varepsilon \ll 1$ to both $q = 0$ and $q = 1$, so that either b or Ψ evolves

as an almost-linear perturbation on a background solution driven by the other field.

We begin with the case $q = 1 - \varepsilon$, with $\varepsilon = 10^{-6}$. When Ψ evolves essentially as a linear perturbation, separation of variables allows us to consistently look for solutions of the scalar test field equation of the form

$$\Psi(\xi, T) = \text{Re}\, e^{\lambda_\Psi T} \hat{\Psi}(\xi, T), \qquad (46)$$

where $\lambda_\Psi = \kappa_\Psi + i\omega_\Psi$ is a complex number and the complex function $\hat{\Psi}(\xi, T)$ is periodic in T with period Δ_B (the same as the background solution). As a result, $e^{-\kappa_\Psi T} \Psi(\xi, T)$ is only quasi-periodic in T, with a discrete spectrum offset by ω_Ψ.

The radius R_{ah} of apparent horizon formation, which has dimension length, scales as

$$R_{\text{ah}}(p) \sim (p - p_*)^{\gamma_B}. \qquad (47)$$

By applying (46) to the expression for R_Ψ, which has dimension length^{-2}, we deduce that it scales as $\sim e^{2(1+\kappa_\Psi)T}$ when the scalar field is treated perturbatively. For near-critical solutions, the maximum value of curvature is achieved just after departing from self-similarity, which occurs at a time $T \simeq -\gamma_B \ln |p - p^*|$ [14]. From this we obtain the scaling relation

$$\left(\max_{\xi, T} R_\Psi \right)^{-1/2} \sim (p - p_*)^{(1+\kappa_\Psi)\gamma_B}. \qquad (48)$$

The critical exponents $\gamma_B \simeq 0.164$ and $\tilde{\gamma}_\Psi = (1 + \kappa_\Psi)\gamma_B \simeq 0.133$ were calculated from the mass and curvature scaling laws for $q = 1 - \varepsilon = 1 - 10^{-6}$ (Fig. 2), giving us $\kappa_\Psi \simeq -0.19$.

The perturbation exponent κ_Ψ was independently estimated by adjusting $\Psi e^{-\kappa_\Psi T}$ by eye to be as quasi-periodic as possible in our best near-critical evolution, placing it in the interval $\kappa_\Psi \in (-0.2, -0.15)$ (see Fig. 6).

Fig. 3 shows the residuals of the linear fit of the scaling law for R_{ah}

$$\text{res}(p) := \log_{10} R_{\text{ah}} - \gamma \log_{10} |p - p_*| - \beta, \quad (49)$$

where β is the intercept of the fit. Similar plots for $R_B^{-1/2}$ and $R_\Psi^{-1/2}$ are shown in Figs. 4-5.

The quantities Ψ, B/ξ^2 and M/R^2 are represented in Figs. 6-8 for the best subcritical evolution for Gaussian initial data. Both B and B/ξ^2 are dimensionless, but B is $O(R^2)$ near the origin while B/ξ^2 is $O(1)$, which is why we plot the latter. Note that because ϵ is small, at this resolution Figs. 3, 4, 7 and 8 are indistinguishable from their counterparts in the pure gravitational wave case $q = 1$, so they can serve to illustrate that case, too.
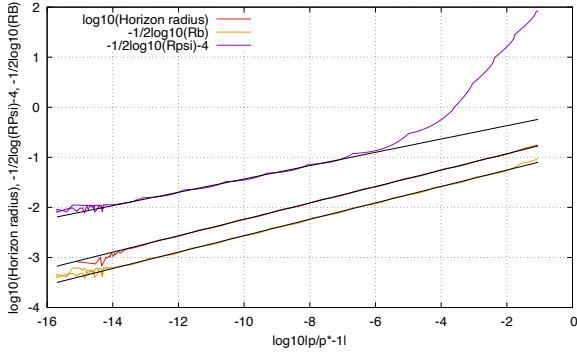
FIG. 2. Scaling laws for the radius R_{ah} of apparent horizon formation, and the global maximum of the Ricci scalar R_Ψ and of R_B for the case $q = 1 - \varepsilon$ and Gaussian initial data. These two last quantities are rescaled by $-1/2$ in the log plot to account for their dimension length^{-2}. The black lines represent the linear fits to each curve. The slope of the lines fitted against R_{ah} and $R_B^{-1/2}$ are 0.1638, and 0.133 for $R_\Psi^{-1/2}$.
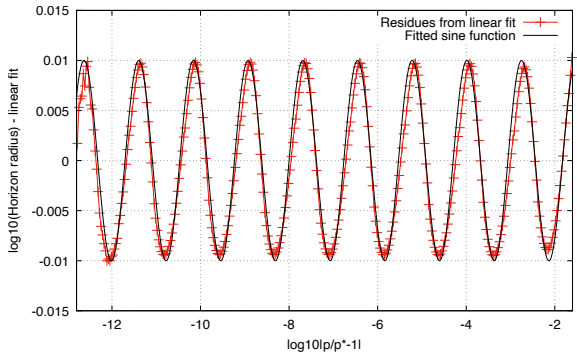
FIG. 3. Residuals of the linear fit to Fig. 2 for the radius R_{ah} of apparent horizon formation for $q = 1 - \varepsilon$. The scaling exponent is $\gamma = 0.1638$ and the fitted period of the residuals is $\Delta_{res} = 1.235$, which is related to the echoing period of the critical solution by $\Delta_{res} = \Delta_B/(\ln(10)\gamma)$, resulting in $\Delta_B \simeq 0.47$, consistent with Fig. 8.

D. Scalar field with small gravitational wave perturbation

Similar calculations hold for B and R_B when $q = \varepsilon = 10^{-6}$, where the gravitational waves are treated as a linear perturbation on the dominant scalar field solution, giving us

$$B(\xi, T) = \text{Re } e^{\lambda_B T} \hat{B}(\xi, T), \qquad (50)$$

with $\lambda_B = \kappa_B + i\omega_B$. The critical exponent $\gamma_\Psi \simeq 0.413$ was calculated numerically from the scaling laws for the radius of apparent horizon formation and for the Ricci scalar, see Fig. (9). The perturbation exponent κ_B was estimated by ad-
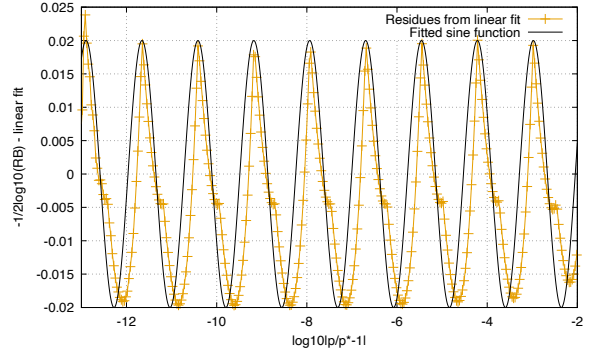
FIG. 4. Residuals of the linear fit to Fig. 2 for R_B for $q = 1 - \varepsilon$. The scaling exponent is $\gamma = 0.1638$ and the fitted period of the residuals is $\Delta_{res} = 1.24$, resulting in $\Delta_B \simeq 0.47$, consistent with Fig. 7.
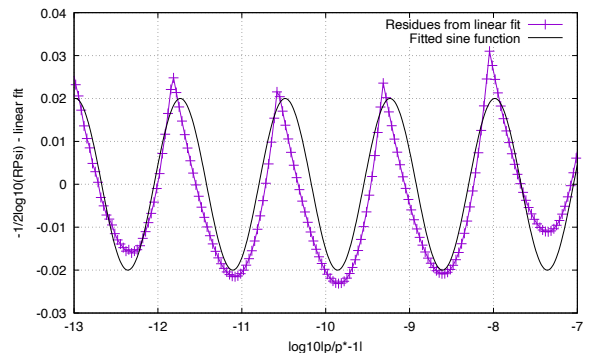
FIG. 5. Residuals of the linear fit to Fig. 2 for the Ricci scalar R_Ψ for $q = 1 - \varepsilon$. The scaling exponent is $\gamma = 0.133$ and the fitted period of the residuals is $\Delta_{res} = 1.25$.
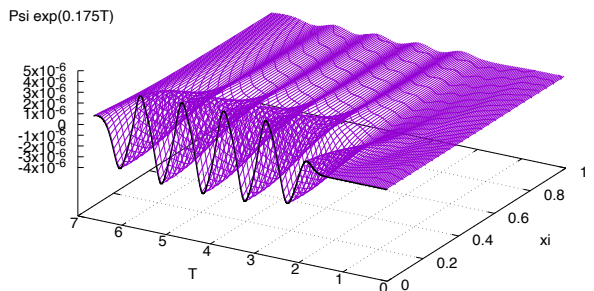
FIG. 6. The scalar field $\Psi(\xi, T)e^{-\kappa_\Psi T}$ for optimal fine-tuning with $q = 1 - \varepsilon$, $\kappa_\Psi = -0.175$. A black line represents the extrapolation to the regular centre $R = 0$.

justing $Be^{-\kappa_B T}$ by eye to be as periodic as possible in our best near-critical evolution, placing it in the interval $\kappa_B \in (-1.55, -1.45)$. The maximum of the pseudo-curvature R_B does not show power law scaling in $(p-p_*)$: R_B scales as $\sim e^{2(1+\kappa_B)T}$, which decays because $\kappa_B < -1$, and so its global maxi-

8
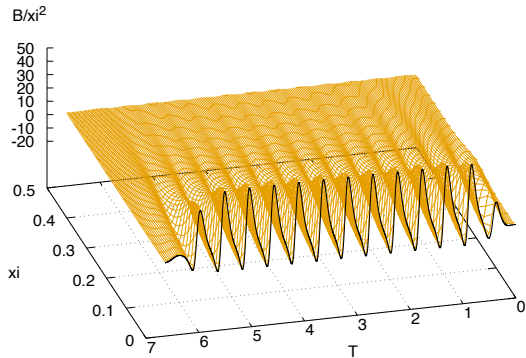
FIG. 7. The quantity B/ξ^2 for optimal fine-tuning with $q = 1 - \varepsilon$. A black line represents the extrapolation to the regular centre $R = 0$.

FIG. 8. The compactness M/R^2 for optimal fine-tuning with $q = 1 - \varepsilon$.

FIG. 9. Scaling laws for the radius R_{ah} of apparent horizon formation, and the global maximum of the Ricci scalar R_Ψ for the case $q = \varepsilon$ and Gaussian initial data. The latter is rescaled by $-1/2$ in the log plot to account for its dimension length^{-2}. The black lines represent the linear fits to each curve. The slope of the lines fitted against R_{ah} and $(R_\Psi)^{-1/2}$ were 0.4131.
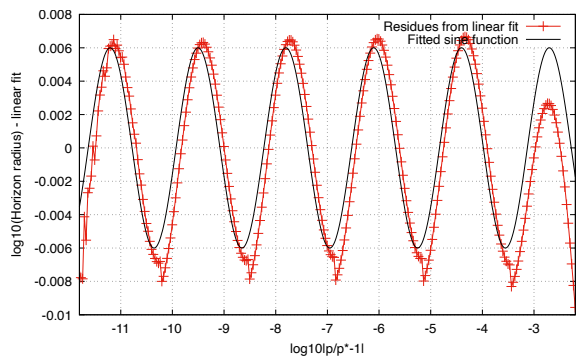
FIG. 10. Residuals of the linear fit to Fig. 9 for the for the radius R_{ah} of apparent horizon formation for $q = \varepsilon$. The scaling exponent is $\gamma = 0.4131$ and the fitted period of the residuals is $\Delta_{\mathrm{res}} = 1.7$, which is related to the echoing period of the critical solution by $\Delta_{\mathrm{res}} = \Delta_\Psi/(\ln(10)\gamma)$, resulting in $\Delta_\Psi \simeq 1.6$, consistent with Fig. 14.

mum is dominated by a value at early times which is dependent on the initial data, and so one cannot apply the same argument that led to Eq. (48).

The residuals of the linear fit for the scaling laws of R_{ah} and $R_\Psi^{-1/2}$ are represented in Figs. 10-11. The quantities $\Psi, B/\xi^2$ and M/R^2 are represented in Figs. 12-14 for the best subcritical evolution for Gaussian initial data. Again, Figs. 10, 11, 12 and 14 are at this resolution indistinguishable from their counterparts in the case $q = 0$ of a pure scalar field.

E. Mixed fields and the bi-critical solution

As κ_B and κ_Ψ have both negative real part, both Ψ and B are decaying perturbations on the background critical solution of the other field when their initial amplitude is sufficiently small such that their dynamics are essentially linear.

When q is decreased more from $q = 1$, the scalar field Ψ still decays, but when $q \lesssim 0.9$ (for Gaussian initial data) the non-linear dynamics play a more significant role and Ψ instead starts growing with

T, with R_Ψ eventually dominating R_B, and the solution approaches the known scalar field critical solution for large enough T. The same behaviour is observed for the other 2-parameter family of initial data, although the value of q for which the scalar field begins to grow with T is $q \lesssim 0.85$. We have investigated the transition between these two regimes, such that the scalar field and the gravitational wave both neither grow nor decay in the critical solution found by fine-tuning p to p_* for given $q \simeq q_*$. In other words, we have to fine-tune in two parameters at once. In practice, we fine-tune to the black-hole threshold $p = p_*(q)$ in an automated inner loop, and fine-tune to q_* in a manual outer loop, as the bisection criterion for q is less clear-cut than collapse versus dispersion for p, and we were not sure what to expect at the q
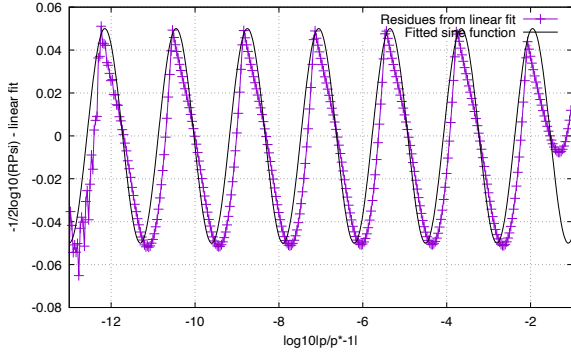
FIG. 11. Residuals of the linear fit to Fig. 9 for the Ricci scalar R_Ψ for $q = \varepsilon$. The scaling exponent is $\gamma = 0.4131$ and the fitted period of the residuals is $\Delta_{\mathrm{res}} = 1.7$, which is related to the echoing period of the critical solution by $\Delta_{\mathrm{res}} = \Delta_\Psi/(\ln(10)\gamma)$, resulting in $\Delta_\Psi \simeq 1.6$, consistent with Fig. 12.
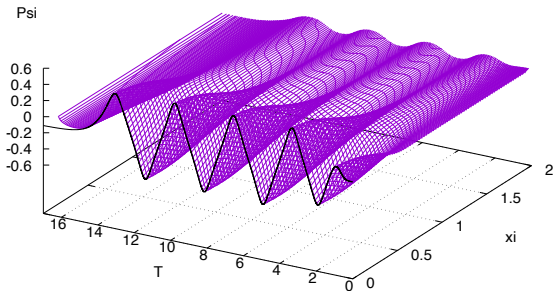
FIG. 12. The scalar field $\Psi(\xi, T)$ for optimal fine-tuning with $q = \varepsilon$. A black line represents the extrapolation to the regular centre $R = 0$.
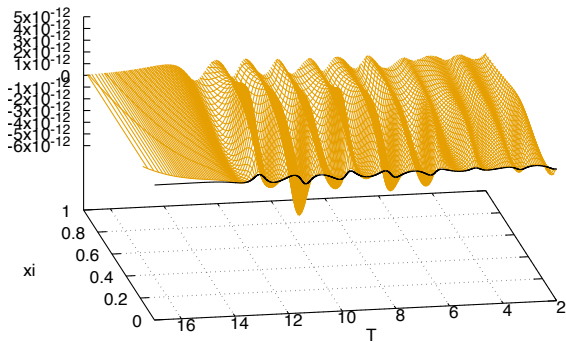
FIG. 13. The quantity $B/\xi^2 e^{-\kappa_B T}$ for optimal fine-tuning with $q = \varepsilon$, $\kappa_B = -1.5$. A black line represents the extrapolation to the regular centre $R = 0$. T is restricted to $[2, 17]$ so as to visualize the exponential correction to B after the dominant scalar field starts to approximate the critical solution.

threshold.

We expect the bi-critical solution to be an intermediate attractor for $(p, q) \simeq (p_*(q_*), q_*)$, in which
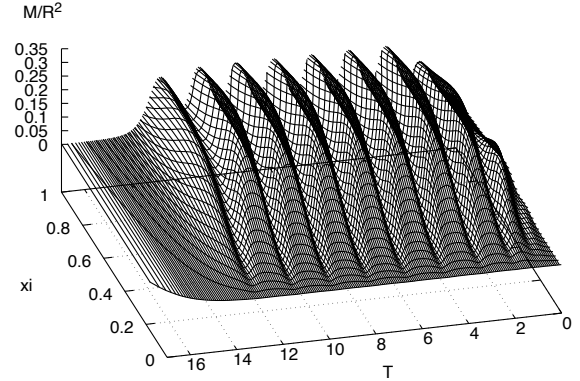
FIG. 14. The compactness M/R^2 for optimal fine-tuning with $q = \varepsilon$.

the solution becomes at least approximately self-similar, with both fields neither growing nor decaying.

In the triaxial vacuum collapse case investigated in [15], for which the two competing fields play symmetric roles (the two critical solutions are the same up to a discrete symmetry), the bi-critical solution was also found to be discretely self-similar with a constant echoing period. In the present biaxial case plus scalar field, however, the two critical solutions are distinct, with $\gamma_\Psi > \gamma_B$ and $\Delta_\Psi > \Delta_B$.

We would have expected that for $q \simeq q_*$ and p sufficiently close to $p_*(q)$, the solution starts out with both b and Ψ equally important. But this is not so at least for our two 2-parameter families. Rather, in these solutions Ψ starts out as a growing perturbation of the b critical solution, before entering a phase where both Ψ and b neither grow nor decay, and spacetime is still approximately DSS.

The presence of this transition phase means that we use up some of the available fine-tuning of p, and hence some of the available range of T, before we reach the expected bi-critical solution. This in turn means that we cannot fine-tune q as well as expected, nor observe the properties of the bi-critical solution over as many periods as expected.

Fig. 15 illustrates the dimensionless quantities $R^2 R_\Psi$ and $R^2 R_B$, which can be taken as measures of how much Ψ and b curve the spacetime, for three different values of q close to the threshold q_*. In Fig. 15a, with $q = q_a \simeq 0.918$, the scalar field grows with T while the solution is approximately DSS, and its stress-energy content dominates R_B, for $T > 3.5$, until both fields eventually disperse (as $p < p_*$ in this evolution). In Fig. 15c, with $q = q_c \simeq 0.922$, the scalar field is decaying while the solution is approximately DSS: the amplitude of $R^2 R_\Psi$ grows until $T \simeq 4.5$ and then it decays while that of $R^2 R_B$ grows until $T \simeq 6$, after which both fields disperse. In Fig. 15b, with the inter-

(a) $q := q_a = 0.9184570312$.

(b) $q := q_b = 0.9200439452$.

(c) $q := q_c = 0.9216308593$.

(d) $q = 0$ (purple) and $q = 1$ (orange).
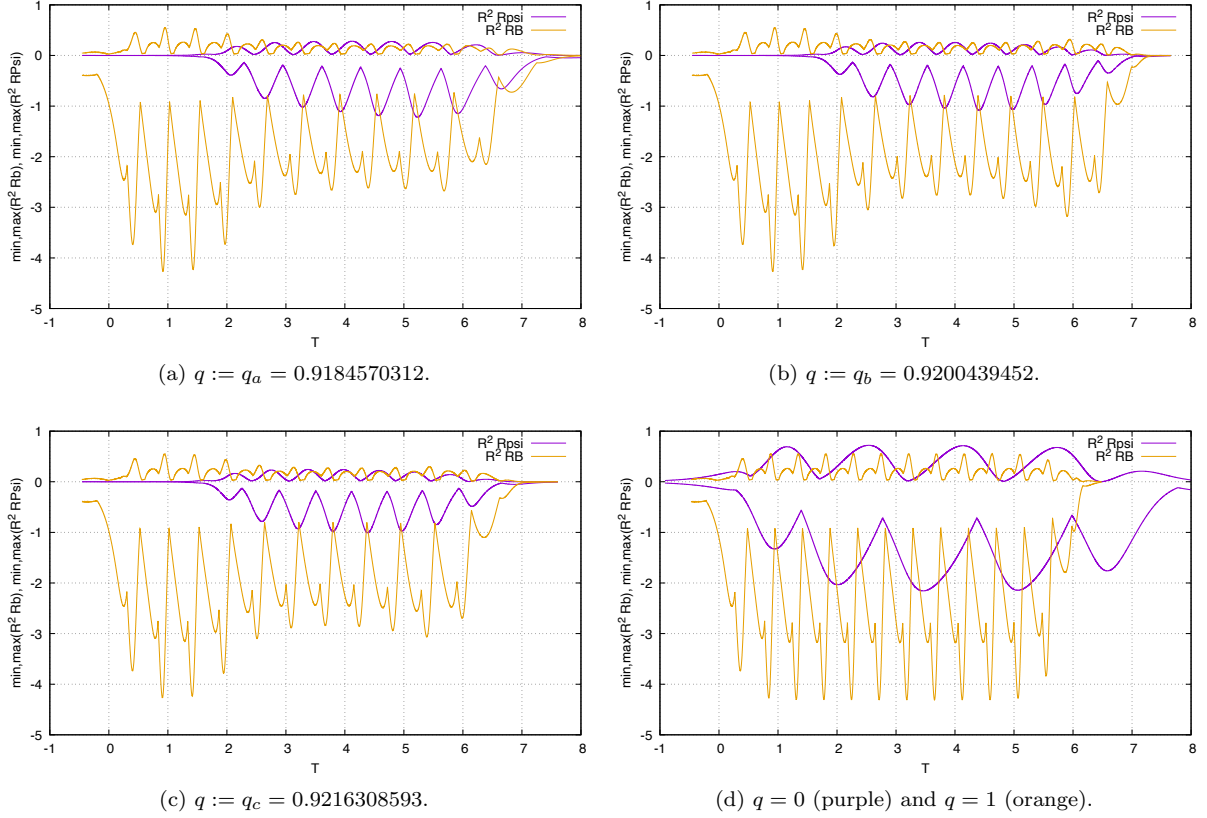
FIG. 15. The maxima and minima (over x) of the quantities $R^2 R_B$ (orange) and $R^2 R_\Psi$ (purple), plotted against T for different values of q, with $q_a < q_b < q_c$, extracted from the respective best subcritical evolutions. For reference, the same quantities for the two pure critical solutions are plotted together in Fig. 15d.

mediate value $q = q_b \simeq 0.920$, both fields Ψ and B seem to stay at approximately the same relative amplitude until they both disperse. It is difficult to tell whether Ψ grows or decays because the interval where the solution is approximately DSS is short, and this makes it harder to determine q_* precisely. However, we are confident that $q_a < q_* < q_c$, with $q_* \simeq q_b$ our best approximation (for the Gaussian initial data). To improve the bisection in q, one would need to run our time evolutions in quadruple precision, so as to better fine-tune p_* and thus observe more echoing before the fields disperse or form a black hole. As that is computationally much more time-consuming, we have not attempted it.

For comparison with Figs. 15a-15c, Fig. 15d illustrates $R^2 R_\Psi$ for the pure scalar field critical solution ($q = 0$) and $R^2 R_B$ for the pure gravitational wave critical solution ($q = 1$).

Figs. 16-18 show Ψ, B and M/R^2 for the best subcritical evolution with Gaussian initial data and with $q = q_b$, which was our best estimate of q_* up to two decimal digits. We observe that Ψ and B are approximately neither growing or decaying for $2.5 \le T \le 7$ before dispersing.

From the data underlying these figures, we have estimated the echoing periods of Ψ, B, $\mathcal{C}$, $R^2 R_\Psi$ and $R^2 R_B$ as follows. We take discrete Fourier transforms of $(\max_x \Psi)(T)$ and $(\max_x B)(T)$ for a suitable interval of T, and adjust the resulting period for what seemed the best fit by eye. Although this is subjective, from the quality of the fit we estimate that we can determine the periods within ~ 0.01. The results are given, separately for $\Delta_\Psi/2$ and Δ_B, and for different $q \simeq q_*$, in Tables I and II, respectively.

Although the separately fitted values of $\Delta_\Psi/2$ and Δ_B are not equal, they are roughly within our estimate of the accuracy ~ 0.01 to which we can determine these periods. Note that the variation of the periods with q over the ranges of q considered in the table is somewhat larger than the difference of $\Delta_\Psi/2$ and Δ_B at the same q. (As already discussed, we are not able to determine q_* very accurately.)

As further tests, we have also compared the fitted values of $\Delta_\Psi/2$ and Δ_B to our plots of $R^2 R_\Psi$ and $R^2 R_B$, respectively, and find that they match well. Finally, we are confident that $\Delta_B \lesssim \Delta_\mathcal{C} \lesssim \Delta_\Psi/2$ (consistent with all being equal).

11

TABLE I. Estimated periods $\Delta_\Psi/2$ and Δ_B for Gaussian initial data.

q	$\Delta_\Psi/2$	Δ_B
$0.9184570312 = q_a$	0.61	0.59
$0.9200439452 = q_b$	0.59	0.57
$0.9216308593 = q_c$	0.5825	0.56
0.9248046875	0.574	0.55

TABLE II. Estimated periods $\Delta_\Psi/2$ and Δ_B for Gaussian derivative initial data.

q	$\Delta_\Psi/2$	Δ_B
0.859375	0.5875	0.55
0.8671875	0.56	0.518
0.87	0.55	0.512
0.8725	0.55	0.511

In short, our observations are consistent both with $\Delta_B = \Delta_\Psi/2$ and $\Delta_B < \Delta_\Psi/2$. In other words, we cannot decide if the critical solution is periodic (DSS) or only quasiperiodic in T.

We note, however, that in the system for which this one is a toy model, the Einstein-Maxwell equations in twistfree axisymmetry, all fields in the critical solution are clearly only quasi-periodic [6], already when viewed on their own. By contrast, the quantities in Figs. 16-18 seem, by eye, to be periodic. One may take this to be an argument in favour of strict DSS.

Recall that $\Delta_\Psi \simeq 1.6$ and $\Delta_B \simeq 0.47$ in the pure scalar field and gravitational wave critical solutions, respectively. So we can at least say that $\Delta_\Psi/2$ and Δ_B have moved from their pure values towards a common intermediate value in the bi-critical solution.
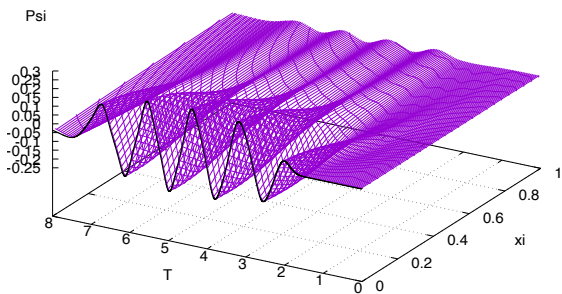
FIG. 16. The scalar field $\Psi(\xi, T)$ for optimal fine-tuning with $q = q_b$. A black line represents the extrapolation to the regular centre $R = 0$.

Fig. 19 illustrates the estimated value of γ for different q, calculated from the scaling laws for the radius of apparent horizon formation R_{ah}. To test universality, we present the results for initial data with a Gaussian profile (in black) and for initial data with the profile of a Gaussian derivative
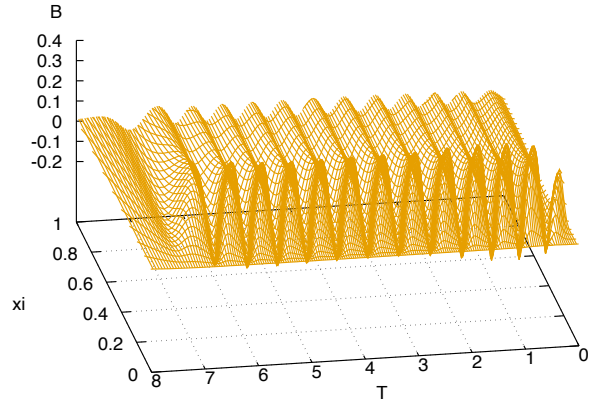
FIG. 17. The field B for optimal fine-tuning with $q = q_b$. It is zero at the origin $R = 0 \Leftrightarrow \xi = 0$ due to Eq. (8).
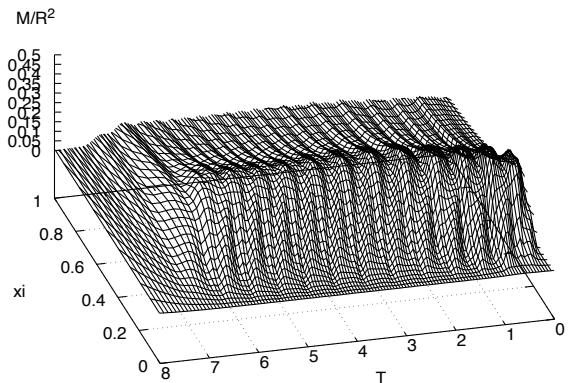
FIG. 18. The compactness M/R^2 for optimal fine-tuning with $q = q_b$.

(in blue). As q_* depends on the family, the black points are plotted against q, and the blue points are plotted against

$$\tilde{q} := \frac{sq}{1 - (1-s)q} \qquad (51)$$

with $0 \leq s \leq 1$ a free parameter. This transformation has $q = 0$ and $q = 1$ as fixed points, with slope 1 near $q = 0$ and slope s near $q = 1$. By adjusting s we can ensure that the neighbourhood around q_* is located approximately at the same region in the $\tilde{q}$-axis for both curves. We have set $s = 0.5$.

From Fig. 19 we see that for both our 2-parameter families of initial data, $\gamma \simeq 0.41$ for $q = 0$, corresponding to the scalar field critical solution, and its does not vary significantly with q until $|q - q_*| \simeq 0.02$. In this interval, the black hole mass scaling exponent depends on $\ln(p - p_*)$: for poor fine-tuning, we find $\gamma \simeq 0.168$, close to gravitational wave critical solution, and for better fine-tuning its value is slightly higher and dependent on q, decreasing monotonically from $\gamma \simeq 0.22$
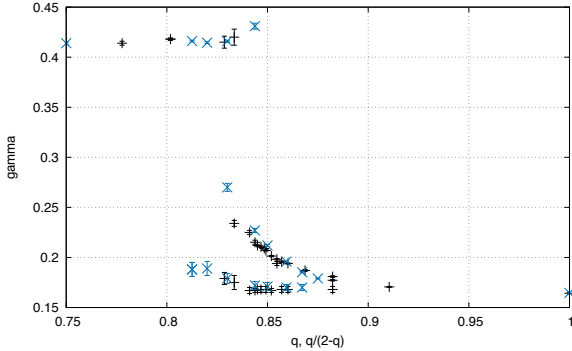
FIG. 19. Plot of the critical exponent γ estimated from the scaling law for radius of apparent horizon formation R_{ah}. The points in black correspond to initial data with a Gaussian profile, which are plotted against q. The points in blue correspond to initial data with the profile of a Gaussian derivative, which are plotted against $sq/(1 - (1 - s)q)$ for $s = 0.5$.

to $\gamma \simeq 0.18$. This break in the scaling laws corresponds to the transition from a growing scalar field perturbation to the true bi-critical solution in near-critical time evolutions, as seen in Figs. 16-18. As q approaches 1, γ settles to the value $\gamma \simeq 0.164$ of the gravitational wave critical solution. For this range of q, the exponent is small, which is why the number of echoing periods seen is limited when fine-tuning in p up to double-precision.

VI. CONCLUSIONS

We have studied the threshold of black hole formation for a massless scalar field minimally coupled to the gravitational wave metric ansatz of [8] in 4+1 dimensions [8], (the latter restricted to the biaxial case). We think of this as a toy model for matter gravitational collapse beyond spherical symmetry, where gravitational waves are also necessarily present.

We found that weak gravitational wave perturbations of the scalar field critical solution decay, while weak scalar perturbations of the gravitational wave critical solution also decay. This is different from the case of critical collapse of two massless matter fields [7], in which scalar perturbations on the Yang-Mills field critical solution grow, but Yang-Mills perturbations on the scalar field critical solution decay.

These observations suggest the schematic phase space picture of Fig. 20. Here, any point in the phase space represents an initial data set, up to an overall length scale, parameterised in our case as $(\Psi(x), \chi(x))$, and a time evolution curve corresponds to a spacetime, in our case in null slicing, again up to an overall scale, with the time T of the

dynamical system determining the missing scale as e^{-T}. In this picture, a DSS solution should be a closed curve, but for simplicity we represent it as a fixed point.

To find the bi-critical solution suggested by this picture, we then explored the transition between the two pure critical solutions for mixed initial data in our new toy model.

The evidence for the existence of the hypothetical codimension-two attractor comes from the behaviour of our best near-critical [that is, $p \simeq p_*(q)$] evolutions for different values of q. In the limit of perfect fine-tuning of p, as the mixing parameter q decreases from 1, we observe a transition from the gravitational wave critical solution to the scalar field critical solution. By continuity, we expect there to be a q_* such that, in the limit of perfect fine-tuning to $p = p_*(q_*)$, both fields play equal dynamical roles. Increasing or decreasing p an infinitesimal amount above or below the curve $p = p_*(q)$ would push the critical solution to eventual collapse or decay, respectively, while increasing or decreasing q exactly along this curve would push it into decaying into the pure gravitational wave or pure scalar critical solutions, respectively.

The numerical limits of fine-tuning do not allow us to follow the putative bi-critical solution for given q down to arbitrarily large T, but our observations are consistent with the assumption that in the limit $(q, p) = (q_*, p_*(q_*))$, the system evolves toward an intermediate attractor for which Ψ and B neither grow nor decay.

Going beyond that, we want to know if the bi-critical solution is strictly DSS, with a common period for all variables (in the sense that $\Delta_\Psi = 2\Delta_B$), or only quasiperiodic. Unfortunately, because we observe the bi-critical solution over few periods, Figs. 16-18 and Fig. 15b seem to be compatible both with $\Delta_\Psi/2 = \Delta_B$ or with a slightly smaller value of Δ_B.

With solutions of the toy model depending only on radius and time, one might hope to construct a strictly DSS solution (as the hypothetical bi-critical solution) by ansatz, imposing periodic boundary conditions in T with a period Δ to be solved for. Such an ansatz was solved numerically for the spherical scalar field in 3+1 dimensions in [16], and the numerical approximate solution was leveraged into a proof of existence as a real-analytic exact solution in [17]. However, a failure to find an approximate numerical solution of such an ansatz would not prove the absence of an exact DSS solution, as the numerical solution of a highly nonlinear boundary value problem may simply not converge from an initial guess that is too rough. By contrast, it is not clear how one could even make an ansatz of quasi-periodicity.
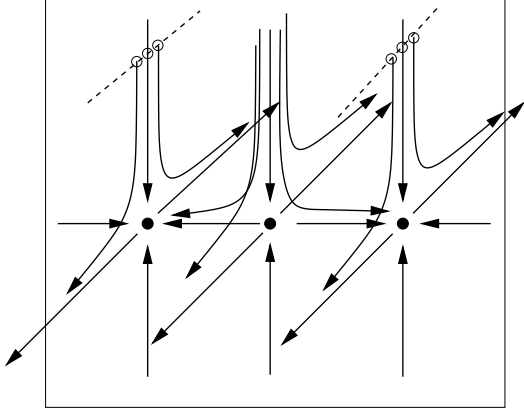
FIG. 20. Schematic conjectured phase space picture, with the infinite-dimensional phase space represented in three dimensions. The framed plane represents the black hole threshold (in reality a hypersurface). All arrow lines represent trajectories (spacetimes). The filled dots represent fixed points (DSS spacetimes): the scalar field critical solution, on the left, the gravitational wave critical solution, on the right, and the codimension-two critical solution in between. Here the middle fixed point has two unstable modes, while the left and right ones have one each. An infinite number of phase space dimensions of the black hole threshold are suppressed, and with them an infinite number of stable modes of each fixed point within the black hole threshold. The two dashed lines represent three families of initial data with $q = 0$ (left) and $q = 1$ (right). Hollow dots represent initial data with $p < p_*$, $p = p_*$ and $p > p_*$ for each family. Figure taken from [7].

Appendix A: Scalar field equations in spherical symmetry in $n + 2$ dimensions

In this Appendix, we explore the problem of a massless scalar field minimally coupled to gravity in a spherically symmetric spacetime in $n + 2$ dimensions. We use coordinates (u, x, Ω_n), where u and x are the same as defined in Section II, and Ω_n are coordinates on the n-sphere:

$$ds^2 = -2gR_{,x}dudx - Hdu^2 + R^2 d\Omega_n^2 \quad (A1)$$

The Einstein equations

$$R_{ab} = 8\pi \nabla_a \Psi \nabla_b \Psi \quad (A2)$$

and the scalar field wave equation

$$\nabla^a \nabla_a \Psi = 0 \quad (A3)$$

can be put in the following hierarchy in these coordinates:

$$\mathcal{D}(\ln g) = \frac{8\pi R}{n}(\mathcal{D}\Psi)^2, \quad (A4)$$

$$\mathcal{D}(R^{n-1}\Xi R) = -\frac{n-1}{2}gR^{n-2}, \quad (A5)$$

$$\mathcal{D}(R^{n/2}\Xi\Psi) = -\frac{n}{2}R^{n/2-1}\Xi R \mathcal{D}\Psi. \quad (A6)$$

Using boundary conditions at $R = 0$, we write the above equations in integral form to make the link to the numerical integrations more explicit:

$$g = \exp\left[\frac{4\pi}{n}\int_0^R (\mathcal{D}\Psi)^2 d(\tilde{R}^2)\right], \quad (A7)$$

$$\Xi R = -\frac{1}{2}\frac{1}{R^{n-1}}\int_0^R g\,d(\tilde{R}^{n-1}), \quad (A8)$$

$$\Xi\Psi = -\frac{1}{R^{n/2}}\int_0^R \mathcal{D}\Psi\Xi R\,d(\tilde{R}^{n/2}). \quad (A9)$$
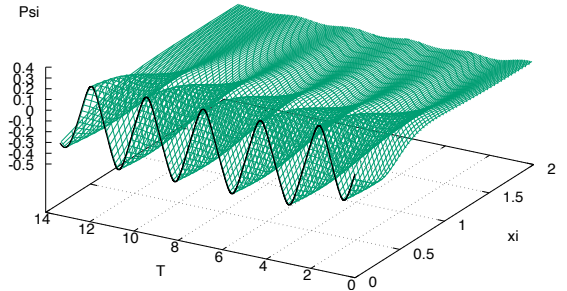
FIG. 21. The scalar field $\Psi(x, T)$ in the best near-critical evolution in 8+1 dimensions. A black line represents the extrapolation to the regular centre $R = 0$.
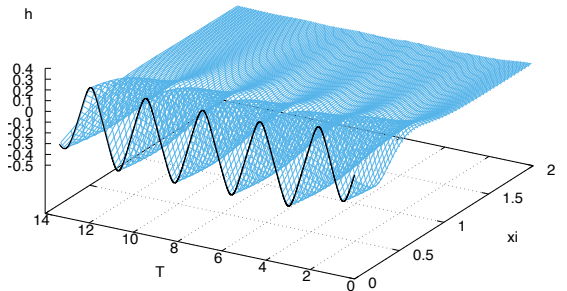
FIG. 22. The field $h(x, T)$ in the best near-critical evolution in 8+1 dimensions. A black line represents the extrapolation to the regular centre $R = 0$.

The division by R^{n-1} to calculate ΞR in Eq. (A8) generates numerical instabilities near the origin $R = 0$ when the dimension increases. While it produces no significant effect in $n + 2 \leq 5$ dimensions, in 8+1 dimensions it leads to unphysical behavior in ΞR. A simple solution to this is to integrate the equation by parts as suggested in [9] and to use Eq. (A7):

$$\Xi R = \frac{g}{2} + \frac{4\pi}{n(n+1)}\frac{1}{R^{n-1}}\int_0^R g(\mathcal{D}\Psi)^2 d(\tilde{R}^n) \quad (A10)$$

The second term in Eq. (A10) can be more accurately computed as it is $O(R^2)$ near the origin.
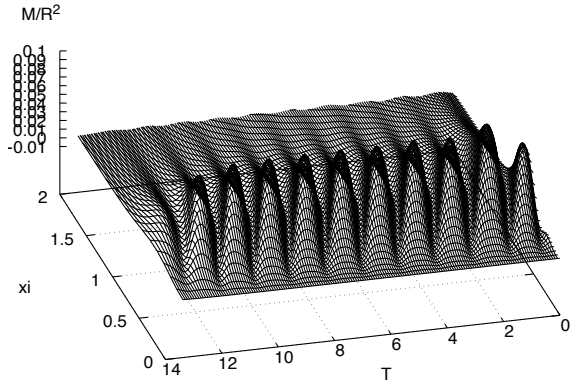
FIG. 23. The compactness M/R^2 in the best near-critical evolution in 8+1 dimensions. A black line represents the extrapolation to the regular centre $R = 0$.

In a similar manner, the wave equation, Eq. (A9), displays instabilities in 8+1 dimensions near the origin $R = 0$ which arise from integrating over and dividing by $R^{n/2}$ the term on the right hand side, which is $O(1)$ for small R. To avoid this, we define a field h as

$$h := \frac{d(R^{n/2}\Psi)}{d(R^{n/2})} = \Psi + \frac{2}{n}(\mathcal{D}\Psi)R, \qquad \text{(A11)}$$

from which we can recover

$$\Psi = \frac{1}{R^{n/2}} \int_0^R h \, d(\tilde{R}^{n/2}). \qquad \text{(A12)}$$

(An evolution equation for h follows below). The problematic integral in Eq. (A9), which is no longer needed, appears to have simply been replaced by another problematic integral, Eq. (A12). However, this can again be integrated by parts to make it more explicitly regular, whereas integration by parts would not be useful for Eq. (A9).

The final form of our field equations can be col-

lected in the following hierarchy:

$$\Psi = h - \frac{1}{\frac{n}{2} + 1} \frac{1}{R^{n/2}} \int_0^R \mathcal{D}h \, d(\tilde{R}^{n/2+1}), \quad \text{(A13)}$$

$$g = \exp\left[\int_0^R 2\pi n \frac{(h - \Psi)^2}{\tilde{R}} \, d(\tilde{R}) \right], \qquad \text{(A14)}$$

$$\Xi R = \frac{g}{2} + \frac{4\pi}{n(n+1)} \frac{1}{R^{n-1}} \int_0^R g(\mathcal{D}\Psi)^2 \, d(\tilde{R}^n), \qquad \text{(A15)}$$

$$\Xi h = \frac{1}{2R}(h - \Psi)\left[(n-1)g + \frac{n}{4}\Xi R \right]. \qquad \text{(A16)}$$

The second term on the right hand side of Eq. (A13) below is $O(R)$ at the origin, and thus more stable to compute than $\Xi\Psi$. [It is not useful to integrate the expression for $\Xi\Psi$ in Eq. (A9) by parts directly, as the integrand would involve second-order derivatives of Ψ.] The new evolution equation (A16) does not require an integral and does not come with high powers of R. Eqs. (A14) and (A16) are well defined at the origin as $h - \Psi = O(R)$ by Eq. (A11) and by regularity of Ψ. In $n + 2 = 4$ dimensions in particular, it is $O(R^2)$ and reduces to $\Xi h = 0$ in Minkowski spacetime, where $g = -\Xi R/2 = 1$.

This field transformation has been commonly used in 4 dimensions, for example in [10–12]. In [18], Garfinkle *et al.* introduced a generalization of h from 3+1 to higher spacetime dimensions, completely different from Eq. (A12), that maintains the property of h being constant along ingoing light rays in Minkowski spacetime, $\Xi h = 0$. This is possible only for even n, as solutions of the wave equation in flat spacetime satisfy Huygens' principle only in even spacetime dimensions. We have tried to explain in this Appendix why the definition of h of Bland *et al.* [9] is numerically advantageous even though for $n \neq 2$ it does not have the very property that seems to have motivated its introduction in $n = 2$.

As an indication that our implementation of this formulation works, Figs. 21-23 show the critical solution in 8+1-dimensional spherical scalar field collapse, found by fine-tuning the amplitude of a family of initial data to the collapse threshold.

In the main paper, we are concerned with the dynamics of the field b, whose governing equation is mathematically similar to that of the scalar wave equation in 8+1 dimensions. As in odd spacetime dimensions we cannot use the methods of [18], we have adopted the formulation described here for arbitrary integer n, with our χ and b in 4+1 dimensions the equivalents of h and Ψ in 8+1 dimensions.

[1] C. Gundlach and J. M. Martín-García, Living Reviews in Relativity **10** (2007).

[2] T. W. Baumgarte, Phys. Rev. D **98**, 084012 (2018).

[3] T. W. Baumgarte and C. Gundlach, Phys. Rev. Lett. **116**, 221103 (2016).

[4] I. Suárez Fernández, S. Renkhoff, D. Cors Agulló, B. Brügmann, and D. Hilditch, "Evolution of brill waves with an adaptive pseudospectral method," arXiv:2205.04379.

[5] T. Ledvinka and A. Khirnov, Phys. Rev. Lett. **127**, 011104 (2022).

[6] T. W. Baumgarte, C. Gundlach, and D. Hilditch, Phys. Rev. Lett. **123**, 17103 (2019).

[7] C. Gundlach, T. W. Baumgarte, and D. Hilditch, Phys. Rev. D **100**, 104010 (2019).

[8] P. Bizoń, T. Chmaj, and B. G. Schmidt, Phys. Rev. Lett. **95**, 071102 (2005).

[9] J. Bland, B. Preston, M. Becker, G. Kunstatter, and V. Husain, Class. and Quantum Gravity **22**, 5355–5364 (2005).

[10] D. Garfinkle, Phys. Rev. D **51**, 5558–5561 (1995).

[11] D. S. Goldwirth and T. Piran, Phys. Rev. D **36**, 3575–3581 (1987).

[12] C. Gundlach, R. H. Price, and J. Pullin, Phys. Rev. D **49**, 883–889 (1994).

[13] R. Gómez, P. Papadopoulos, and J. Winicour, Journal of Mathematical Physics **35**, 4184–4204 (1994).

[14] S. Hod and T. Piran, Phys. Rev. D **55**, R440–R442 (1997).

[15] P. Bizoń, T. Chmaj, and B. G. Schmidt, Phys. Rev. Lett. **97**, 131101 (2006).

[16] C. Gundlach, Phys. Rev. Lett. **75**, 3214 (1995).

[17] M. Reiterer and E. Trubowitz, Commun. Math. Phys. **368**, 143 (2019).

[18] D. Garfinkle, C. Cutler, and G. Comer Duncan, Phys. Rev. D **60**, 104007 (1999).